

This copy is for your personal, non-commercial use only.

If you wish to distribute this article to others, you can order high-quality copies for your colleagues, clients, or customers by [clicking here](#).

Permission to republish or repurpose articles or portions of articles can be obtained by following the guidelines [here](#).

The following resources related to this article are available online at www.sciencemag.org (this information is current as of April 6, 2010):

Updated information and services, including high-resolution figures, can be found in the online version of this article at:

<http://www.sciencemag.org/cgi/content/full/328/5974/76>

Supporting Online Material can be found at:

<http://www.sciencemag.org/cgi/content/full/328/5974/76/DC1>

This article **cites 28 articles**, 4 of which can be accessed for free:

<http://www.sciencemag.org/cgi/content/full/328/5974/76#otherarticles>

This article has been **cited by** 1 articles hosted by HighWire Press; see:

<http://www.sciencemag.org/cgi/content/full/328/5974/76#otherarticles>

This article appears in the following **subject collections**:

Physics, Applied

http://www.sciencemag.org/cgi/collection/app_physics

Frictional Characteristics of Atomically Thin Sheets

Changgu Lee,^{1*} Qunyang Li,^{2*} William Kalb,¹ Xin-Zhou Liu,³ Helmuth Berger,⁴ Robert W. Carpick,^{2†} James Hone¹

Using friction force microscopy, we compared the nanoscale frictional characteristics of atomically thin sheets of graphene, molybdenum disulfide (MoS₂), niobium diselenide, and hexagonal boron nitride exfoliated onto a weakly adherent substrate (silicon oxide) to those of their bulk counterparts. Measurements down to single atomic sheets revealed that friction monotonically increased as the number of layers decreased for all four materials. Suspended graphene membranes showed the same trend, but binding the graphene strongly to a mica surface suppressed the trend. Tip-sample adhesion forces were indistinguishable for all thicknesses and substrate arrangements. Both graphene and MoS₂ exhibited atomic lattice stick-slip friction, with the thinnest sheets possessing a sliding-length-dependent increase in static friction. These observations, coupled with finite element modeling, suggest that the trend arises from the thinner sheets' increased susceptibility to out-of-plane elastic deformation. The generality of the results indicates that this may be a universal characteristic of nanoscale friction for atomically thin materials weakly bound to substrates.

The development of materials and structures with nanoscale features highlights the need to understand how such materials behave in contact. The high relative surface area at small scales renders adhesion, friction, and wear consequential for nanoscale data storage de-

vices, nanocomposites, and nanoelectromechanical systems (NEMS). Two-dimensional (2D) architectures are of particular interest, because their planar geometry is compatible with wafer-level processing. How material behavior depends on structural dimensionality is relevant scientifically,

particularly at the nanoscale: Quasi-0D materials (quantum dots, nanoparticles) and quasi-1D materials (nanowires, nanotubes) behave very differently from their 3D counterparts (1, 2). Studies of isolated atomic sheets have demonstrated the distinct properties of 2D materials as well. The most widely studied of these is graphene, which exhibits notable electronic, thermal, chemical, and mechanical properties including unrivaled mechanical stiffness and strength (3). This motivates considering graphene for next-generation electronic devices and NEMS (4, 5).

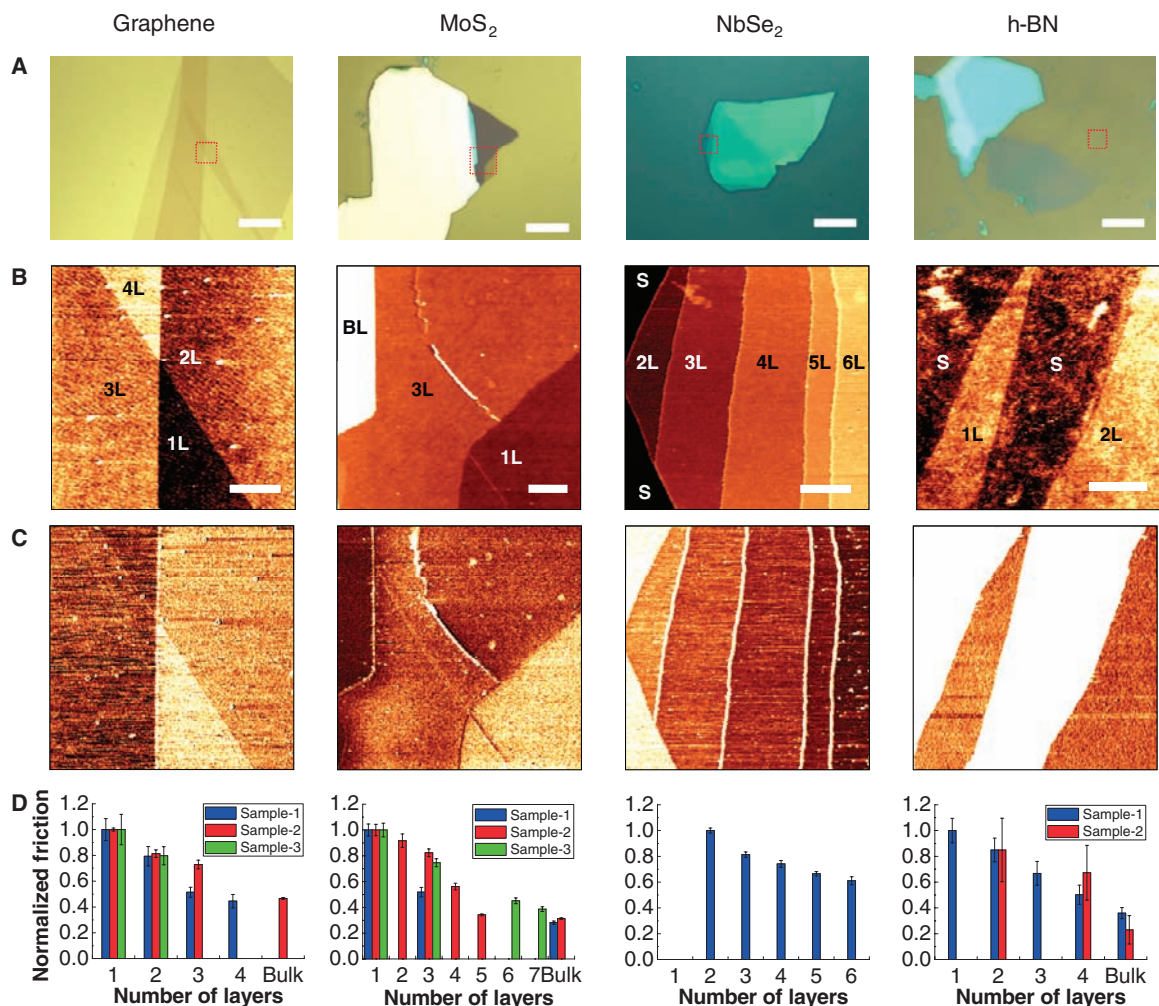
For such applications, the mechanical and tribological properties of these materials must be better understood. To this end, four atomically-thin quasi-2D materials—graphene, molybdenum disulfide (MoS₂), hexagonal boron nitride (h-BN), and niobium diselenide (NbSe₂)—were separated

¹Department of Mechanical Engineering, Columbia University, New York, NY 10027, USA. ²Department of Mechanical Engineering and Applied Mechanics, University of Pennsylvania, Philadelphia, PA 19104, USA. ³Department of Physics, Leiden University, 2300 RA Leiden, Netherlands. ⁴Institute of Physics of Condensed Matter, Ecole Polytechnique Fédérale de Lausanne, CH-1015 Lausanne, Switzerland.

*These authors contributed equally to this work.

†To whom correspondence should be addressed. E-mail: carpick@seas.upenn.edu

Fig. 1. Optical and AFM images of atomically thin sheets of (from left to right) graphene, MoS₂, NbSe₂, and h-BN on silicon oxide. (A) Bright-field optical microscope images of thin sample flakes. The red dotted squares represent subsequent AFM scan areas. Scale bars, 10 μm. (B and C) Topographic and friction (forward scan) images measured simultaneously by AFM from the indicated areas. 1L, 2L, 3L, etc., indicate sheets with thicknesses of one, two, three, etc., atomic layers. BL (“bulk-like”) denotes an area with a very thick flake, and S represents an area with bare SiO₂ substrate. Scale bars, 1 μm. (D) Friction on areas with different layer thicknesses. For each sample, friction is normalized to the value obtained for the thinnest layer. Error bars represent the standard deviation of the friction signals of each area. In each chart, the same color represents data from the same sample.



from their bulk sources by mechanical exfoliation (6) and their nanotribological properties characterized by friction force microscopy (FFM). These materials have widely varying electronic properties: NbSe₂ is metallic; graphene is a zero-bandgap semiconductor or a semimetal (depending on thickness); MoS₂ is a semiconductor; and h-BN is insulating.

The bulk analogs of these lamellar materials, particularly graphite, MoS₂, and h-BN, are widely used as solid lubricant films in critical engineering applications (7, 8). The way in which asperities interact with the lamellar structures in these films, and how lamellae interact with each other, are key areas where molecular-level insights could be valuable.

Recently, FFM measurements found that monolayer epitaxial graphene on SiC exhibits higher friction than bilayer graphene (9). Here, we observe that friction on all four quasi-2D materials studied is higher than that of their bulk counterparts. The evolution from monolayer to multiple layers and bulk is quantitatively studied at the micrometer scale and at the atomic-level stick-slip regime. The experiments, and finite element modeling, indicate that the higher friction is related to the low bending stiffness of the thinnest layers.

Graphene, MoS₂, h-BN, and NbSe₂ flakes were deposited in ambient conditions by mechanically exfoliating bulk source materials onto SiO₂/Si (SiO₂: 300 nm) substrates in a manner similar to that previously established (6). After deposition, the samples did not go through any further treatment, so as-deposited materials were used for all measurements. The thinnest flakes were identified by optical microscopy (Fig. 1A). The exfoliated flakes have typical lateral dimensions of tens of micrometers, consisting of both thin and thick areas.

Micrometer-scale imaging and FFM were performed in contact mode with a Park Systems XE-100 atomic force microscope (AFM) in an ambient environment (25 to 50% relative humidity, 20° to 25°C, unless otherwise noted). Silicon AFM probes [Mikromasch CSC17, specified tip radius $R = 5$ to 10 nm, and typical normal force constant $k \approx 0.15$ N/m, calibrated using the reference cantilever method (10)] were used at an applied force of 1 nN with scan areas several micrometers across. Contact-mode AFM is a

reliable method for providing accurate height measurements of atomically thin sheets (11). Thicknesses of the monolayer sheets closely matched the interlayer crystal spacings of each material (0.335, 0.615, 1.288, and 0.333 nm for graphene, MoS₂, NbSe₂, and h-BN, respectively). Thicker multilayered regions had thicknesses close to integer multiples of the interlayer spacings (fig. S1) (12). The topographic AFM images of the thin flakes are shown in Fig. 1B. The regions labeled 1L, 2L, etc., correspond to where the flakes are one-layer, two-layer, etc., thick. Regions labeled BL are very thick (bulk-like, >20 layers). For graphene, the measured thicknesses were independently confirmed by Raman spectroscopy (13).

FFM images (Fig. 1C), obtained simultaneously with the topographic images, show a pattern of increasing friction with decreasing thickness. To quantify the observed trend, we calculated the friction force by dividing the friction signal difference between the steady-state values in the forward and reverse scans by two. For all four materials, the friction force is roughly equal to the bulk value for samples thicker than about five layers and increases monotonically with decreasing thickness below that point (Fig. 1D). Monolayer sheets show ~20% greater friction than bilayer sheets, and two to three times higher friction than bulk sheets. Extrinsic factors that can affect the measured friction—, such as tip size, shape, and composition, applied load, environment, and scan speed (14)—, are kept constant for a given image; for each data set we report friction normalized to the value measured on the thinnest sheet found (one or two layers depending on the material). We also obtained absolute friction values on thick areas (>10 layers) of the four materials with a Si tip calibrated by a diamagnetic lateral force calibrator (12, 15) (fig. S2). We observed that graphene, MoS₂, and h-BN had much lower friction (~1 nN) than NbSe₂ (~7 nN).

The trend of increasing friction with decreasing thickness was robust over a large range of experimental conditions. The results were reproduced when distinct Si tips and samples were used for all four materials. The trend did not depend on scan speed from 1 to 10 $\mu\text{m/s}$, or on normal load from 0.1 to 2 nN. The trend was also seen in graphene for a normal load of 50 nN

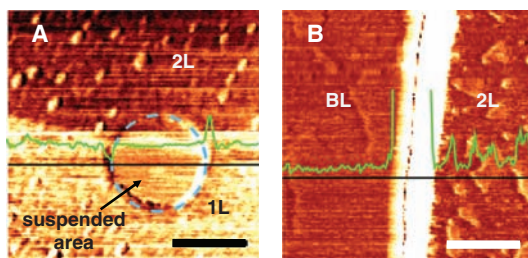
when a stiffer silicon nitride-coated probe was used [DP15/LS, nonconducting, Mikromasch, $R = 20$ to 30 nm, $k = 45$ N/m, calibrated by Sader's method (16)]. Friction was also measured with tips made of other materials, including silicon nitride (DP15/LS, Mikromasch) and diamond (ND-CTIR1 "NaDia Probe," nonconducting, Advanced Diamond Technologies). The relative changes in friction were comparable for every tip. Reducing the humidity from ~30 to <5% in N₂ for graphene and MoS₂ led to overall lower friction forces (by ~20 to 30%), but the trend with layer thickness was preserved. Because tip-substrate adhesion can influence friction (17), we measured adhesion on samples by carrying out force-displacement spectroscopy. There was no resolvable difference in adhesion between areas of different thicknesses for any of the materials studied.

The observation of increasing friction with decreasing thickness is consistent with experiments on one-layer and two-layer SiC-derived graphene of Filleter *et al.* (9), and extends the trend to more layers and additional materials. However, Filleter *et al.* reported that bulk graphite has higher friction than one-layer and two-layer graphene, whereas we observe that friction on graphene approaches that of graphite as the number of layers increases.

Two experiments were next performed to test the role of the substrate in the friction measurements. First, graphene was deposited on substrates with 300-nm-diameter circular holes to form freely suspended membranes. FFM images showed no difference in friction between the suspended and substrate-supported graphene. Figure 2A shows one such sample, in which areas of one-layer and two-layer graphene were suspended over the same hole. Both thicknesses showed the same behavior when suspended and supported. Second, graphene was deposited on muscovite mica, on which it is strongly adherent and atomically flat because of mica's high surface energy (18). Graphene was deposited within several seconds after the mica was mechanically cleaved to minimize adsorption of water on the surface; little difference in topography and friction was observed for samples deposited in air or in dry nitrogen. As previously reported (18), topographic images [see Supporting Online Material (SOM) (12)] reveal two types of behavior: atomically flat areas in intimate contact with the mica, and slightly (0.2 to 0.3 nm) elevated "bubbles," which appear to be caused by gas trapped between the graphene and mica. Figure 2B shows a FFM image of a thick (~9 nm) graphene flake next to a two-layer flake, separated by a narrow region of bare mica. The friction shown by flat areas of the two-layer region is identical to that of the thick sample, whereas friction shown by the "bubbles" is about twice as large, consistent with behavior on SiO₂ or when suspended.

A second set of measurements was obtained by scanning for only a few nanometers across

Fig. 2. FFM images of suspended graphene (A) and graphene deposited on mica (B). Scale bars, 0.3 μm . The green lines are profiles of friction force along the black scan lines. In (A), there is no difference in friction between the suspended and supported areas for both 1L and 2L graphene, but friction for 2L is noticeably lower than for 1L. In (B), friction for the thick (BL) and 2L graphene (the topographically lower regions) is the same. The 2L graphene possesses isolated regions of higher friction that are topographically elevated and may be due to trapped gas or liquid.



graphene and MoS₂ samples with a RHK UHV350 AFM (Fig. 3). The ultrahigh-vacuum AFM chamber was purged by clean, dry nitrogen (from vaporized liquid nitrogen) and then sealed. The relative humidity was measured to be <5% and was likely around 1 to 2% based on measurements under similar conditions. For graphene, the normal force was maintained at 4 nN with a silicon probe [CSC37 Mikromasch, force constant 0.18 N/m calibrated using Sader's method (16)]. The scan speed was 40 nm/s for 2-nm scan sizes and 100 nm/s for 5-nm scan sizes. For measurements on MoS₂, the normal force was 3.6 nN exerted by a silicon probe (CSC17 Mikromasch, calibrated force constant 0.1 N/m), with scan speeds of 25 nm/s for 5-nm scan sizes and 50 nm/s for 10-nm scan sizes. In both cases, the lateral force was calibrated by a diamagnetic lateral force calibrator (15).

Figure 3A shows line traces of the friction force for 2-nm scan widths. The tip exhibits clear, periodic stick-slip motion, similar to that observed previously for bulk graphite and MoS₂, respectively (19–21). However, on the thinnest sheets, the force at which each slip occurs increases in magnitude during each forward and reverse scan, producing a tilted friction loop. This “strengthening” effect is highlighted by the dotted trend lines in

the figure and is strongest for the monolayer. At longer scan lengths of 5 nm, the strengthening effect saturates as the scan proceeds (Fig. 3B).

Because of this friction strengthening, it is more straightforward to report the relative frictional energy dissipated per unit cell as opposed to the average or maximum force (Fig. 3C). This is obtained by first integrating the friction force over the forward and reverse scans and then dividing the result by the number of apparent unit cells scanned. For both graphene and MoS₂, the energy dissipated per unit cell decreases monotonically with an increase in the number of layers, and approaches that of bulk materials. This is consistent with the micrometer-scale measurements (Fig. 1), although the dependence on thickness is slightly less prominent. This could be due to the different scan velocities, tip sizes or shapes, or environments; detailed studies are needed to fully explore these modest differences. The energy dissipated per slip ranges from ~2.5 to 10 eV, which is initially generated at a contact that spans a diameter of several nanometers and therefore involves several hundreds of atoms at the interface.

Atomic-level stick-slip on bulk graphite and MoS₂ yields friction images with threefold symmetric patterns (22, 23). Representative examples

of raw and filtered friction images on both one-layer and bulk materials are shown in Fig. 3D. The raw friction signal on one-layer sheets appears darker on the left because of the strengthening effect, whereas the force at which slip occurs is uniform for the bulk materials. Similar threefold symmetric patterns were observed for all the samples, corresponding to the known symmetry of the lattices.

During the strengthening portion of the friction loops, the periodicity for graphene is increased along the fast scanning direction, as seen by comparing the lattice measured from one-layer graphene to that from bulk graphite (Fig. 3D, filled circles). This effect gets weaker as the number of layers increases, and the lattice measured from four-layer graphene is nearly indistinguishable from that of bulk graphite (fig. S5). For one-layer MoS₂, a higher level of drift prevented any similar effect from being resolved.

The stick-slip images allow observation of the crystal orientation of each exposed layer. For graphene, the individual stacked region of a given flake all share the same orientation to within 0.4°, which means that the layers of an exfoliated flake remain commensurate. This relatively straightforward FFM imaging technique may prove useful for characterization of

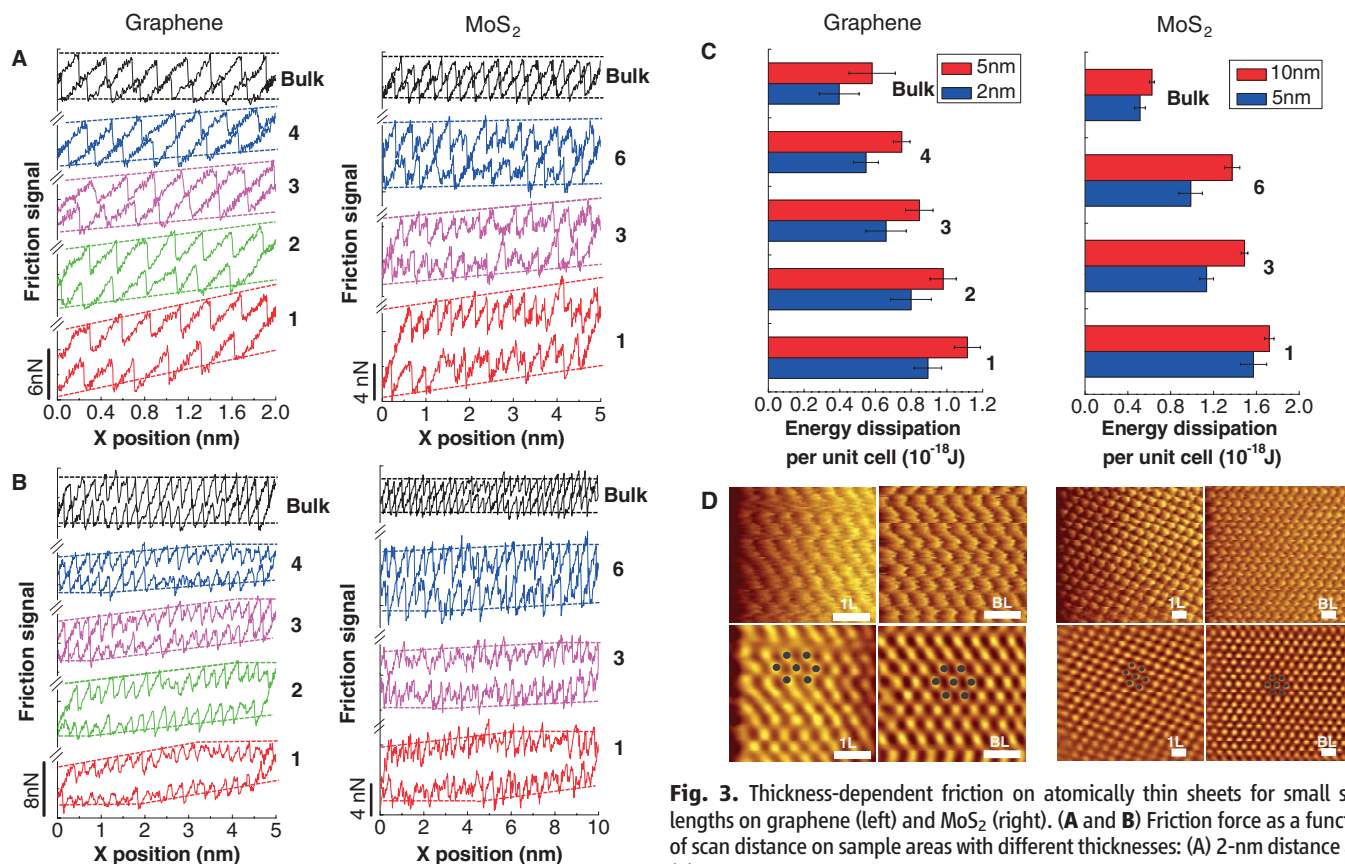


Fig. 3. Thickness-dependent friction on atomically thin sheets for small scan lengths on graphene (left) and MoS₂ (right). **(A and B)** Friction force as a function of scan distance on sample areas with different thicknesses: (A) 2-nm distance and (B) 5-nm scan distance. The numbers on the right indicate the corresponding numbers of atomic layers. The friction traces show that the tip moves unstably with stick-slip motion coupled with an unusual “strengthening” effect, which is highlighted by the dotted trend lines. **(C)** Energy dissipation per unit cell of slip as the tip slides over the thin sheets, as well as over the bulk counterparts. **(D)** Raw (upper) and low-pass filtered (lower) images showing the friction signal in the forward sliding direction for 1L (left) and thick (BL) (right) samples. The filtered images show the periodicity of the lattice; black dots represent the periodic sites of the friction force signal. For graphene, the lattice is clearly stretched in the strengthening portion of the friction measurement. Scale bars, 0.5 nm.

structures such as epitaxial graphene and graphene nanoribbons, whose electronic properties depend on their width and angle relative to the crystal axis, as well as the degree of disorder at the nanoribbon edge (24, 25).

We next examine potential mechanisms that can account for the observed trend of decreasing friction with increasing thickness. The similar behavior for four materials with widely varying electronic and vibrational properties, as well as the strong substrate effects, argues against phononic (26) and electronic dissipation as the cause (27). In particular, the electron-phonon coupling mechanism proposed by Filleter *et al.* cannot account for our results, although our results do not exclude an additional contribution from this mechanism. A recent model of interfacial dislocation-mediated friction (28) assumes 3D crystalline materials on both sides of an infinite interface; our finite-sized amorphous tip in contact with atomically thin sheets is incompatible with this. In addition, chemical mechanisms and wear are not at play, as we see no evidence of bond breaking or other irreversible structural changes. Finally, the identical behavior of suspended and SiO₂-supported graphene rules out roughening or interaction with charge traps in the SiO₂.

A number of factors argue against the presence in these experiments of interlayer sliding, which could reduce friction for thicker samples. The flakes are much larger than the tip-sample contact area (micrometers versus nanometers), and the flake edges may interact more strongly with the substrate owing to the presence of dangling bonds or oxide groups. Therefore, even for an overall weak flake-substrate adhesion, the force required to move an entire flake is far larger than that required to slide the tip relative to the sample. The steady-state atomic-scale stick-slip results clearly demonstrate that relative slip consistently occurs between the tip and the top surface of the graphene. However, a transient amount of local sliding between the topmost layer and the material below could be occurring during the strengthening portion of the friction loop, i.e., for the first few nanometers of sliding

(Fig. 3, A and D), where the lattice is seen to be distorted. However, this effect is most pronounced in the thinnest samples, indicating that transient interlayer sliding is associated with higher, not lower, friction.

We next consider a mechanical origin for the observed effect, namely, that any material becomes more compliant, especially in bending, as it approaches atomic thickness (the flexural rigidity of an elastic is proportional to its thickness cubed). This is consistent with our observations for four distinct materials, as well as the observed substrate effects: suspended or weakly bonded (i.e., on SiO₂) samples will be more compliant than samples strongly adhered to substrates (i.e., graphene on mica).

To understand the role of the sheet stiffness in friction, we consider a simple model of a tip sliding across a flexible membrane. In this case, when the tip makes contact with the top surface, adhesion causes the sheet to easily pucker locally (29) because of the sheet's low bending stiffness compared to its in-plane stiffness. The puckered geometry will be modified at the front edge by tip-sheet friction, as depicted by the cartoon in Fig. 4A. This out-of-plane puckering could explain increased friction because of the increased tip-sheet contact area that results, or because of additional work required to move the puckered region forward. This will become more pronounced as the sheet becomes thinner, and indeed this is observed in finite element modeling.

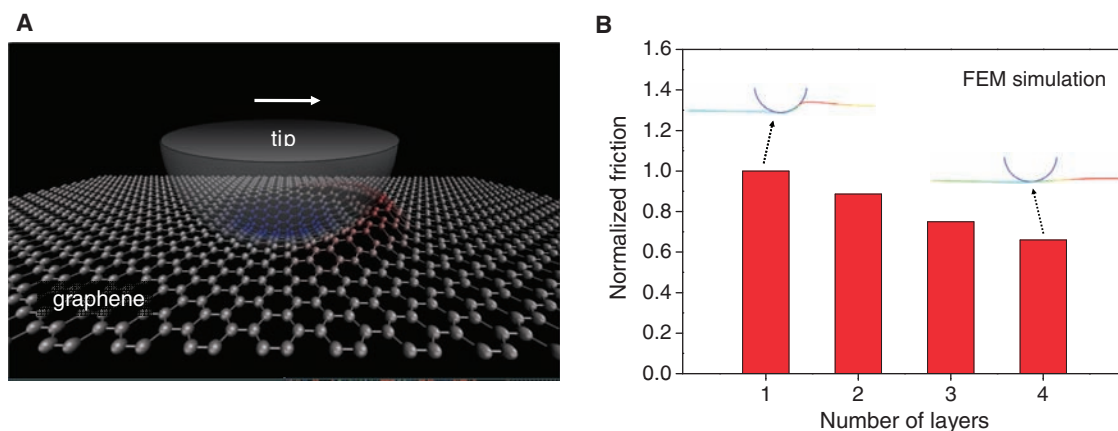
In this picture, one could expect the thinnest sheets to exhibit a transient behavior each time the tip changes direction. The puckered region of the graphene would rearrange under the tip in response to the change in sliding direction. Some relative sliding between the topmost layer and the material below could then occur. This would increase the spacing of the stick-slip events, and this is indeed what is seen during the strengthening portion of the friction loops (Fig. 3, A, B, and D).

To test the puckering idea further, we performed finite element modeling for a simplified 2D continuum model. In the model, a rigid spherical tip is slid over a thin elastic sheet whose bending stiffness and in-plane rigidity are

dependent on its thickness. The tip-sheet interaction is described by an effective adhesive force originating from Lennard-Jones interaction, and a shear stress obtained from contact-size-dependent friction model (see SOM for details) (12). Because of adhesion, the elastic sheet snaps to the tip, and locally puckers if the sheet is thin enough. When the tip slides, the symmetry of the puckered region breaks and it piles up mostly at the front edge of the contact (Fig. 4B, left inset); the geometry reverses when the tip changes direction. The enlarged contact area from out-of-plane deformation requires more force to slide the tip forward. For a thicker sheet, the puckering is less prominent owing to the larger bending stiffness of the sheet (Fig. 4B, right inset), and therefore friction is lower. The resulting variation in friction with sheet thickness is given in Fig. 4B. The qualitative agreement with the experiments suggests that the puckering effect is a feasible mechanism for the thickness-dependent friction behavior.

No atomistic theory specifically formulated for asperity contact with a thin material contains mechanisms that cause friction to increase as the atomic limit of thickness is approached. However, a recent atomistic model for flat interfaces predicts that as a material varies from 3D to 2D geometry, friction against that material increases (30), owing to weaker scaling of elastic stiffness with size in two dimensions combined with the well-known intrinsic property of atomic lattice stick-slip friction: Stick-slip instabilities and the associated increased frictional dissipation occur when the local elastic stiffness becomes weaker than the gradient of the lateral force arising from the corrugated interfacial potential (31). Increased elastic compliance of the puckered thin sheet could therefore be another related aspect contributing to higher friction in these systems. The finite element model presented here is only a first step in analyzing this behavior. Atomistic simulations tailored to these materials and conditions would not only provide substantial further insights into the present experiments, but could potentially provide needed molecular-level insights into the tribological behavior of solid lubricants.

Fig. 4. (A) A schematic showing the proposed puckering effect, where adhesion to the sliding AFM tip creates out-of-plane deformation of a graphene sheet, leading to increased contact area and friction; the color scale of the atoms indicates their out-of-plane positions. (B) The variation in friction as a function of the sheet thickness based on the FEM simulation. Friction is normalized by the value obtained for a one-layer sheet; the insets indicate the local out-of-plane deformation of the sheets (indicated by the color) around the contact areas for sliding over a one-layer sheet and four-layer sheet.



The consistency of the AFM measurements for four different materials strongly suggests that this phenomenon is universal for atomically thin sheets that are loosely adhered to a substrate or freely suspended. This reveals a new mechanism of enhanced friction for quasi-2D materials based on elastic compliance. Because the effect is suppressed when the sheet is attached to a strongly adhering substrate, the results indicate an avenue to controlling nanoscale friction for these materials. Therefore, these results can potentially aid in the rational design and use of materials for nanomechanical applications, including nanolubricants and components in micro- and nanoelectromechanical systems devices.

References and Notes

- H. Park *et al.*, *Nature* **407**, 57 (2000).
- A. I. Yanson, G. R. Bollinger, H. E. van den Brom, N. Agrait, J. M. van Ruitenbeek, *Nature* **395**, 783 (1998).
- A. K. Geim, *Science* **324**, 1530 (2009).
- K. S. Novoselov *et al.*, *Science* **306**, 666 (2004).
- I. Meric *et al.*, *Nat. Nanotechnol.* **3**, 654 (2008).
- K. S. Novoselov *et al.*, *Proc. Natl. Acad. Sci. U.S.A.* **102**, 10451 (2005).
- C. Donnet, A. Erdemir, *Surf. Coat. Tech.* **180-181**, 76 (2004).
- I. L. Singer, H. M. Pollock, *Fundamentals of Friction: Macroscopic and Microscopic Processes* (Kluwer, Dordrecht, Netherlands, 1992).
- T. Filleter *et al.*, *Phys. Rev. Lett.* **102**, 86102 (2009).
- M. Tortorone, M. Kirk, *Proc. Soc. Photo. Opt. Instrum. Eng.* **3009**, 53 (1997).
- P. Nemes-Incze, Z. Osváth, K. Kamarás, L. P. Biró, *Carbon* **46**, 1435 (2008).
- Sample preparation, additional measurement results, and finite element modeling are available as supporting material on Science Online.
- A. C. Ferrari *et al.*, *Phys. Rev. Lett.* **97**, 187401 (2006).
- I. Szlufarska, M. Chandross, R. W. Carpick, *J. Phys. D Appl. Phys.* **41**, 123001 (2008).
- Q. Li, K. S. Kim, A. Rydberg, *Rev. Sci. Instrum.* **77**, 65105 (2006).
- J. E. Sader, J. W. M. Chon, P. Mulvaney, *Rev. Sci. Instrum.* **70**, 3967 (1999).
- K. L. Johnson, *Contact Mechanics* (Cambridge Univ. Press, Cambridge, 1985).
- C. H. Lui, L. Liu, K. F. Mak, G. W. Flynn, T. F. Heinz, *Nature* **462**, 339 (2009).
- C. M. Mate, G. M. McClelland, R. Erlandsson, S. Chiang, *Phys. Rev. Lett.* **59**, 1942 (1987).
- S. N. Medyanik, W. K. Liu, I.-H. Sung, R. W. Carpick, *Phys. Rev. Lett.* **97**, 136106 (2006).
- X. Zhao, S. R. Phillpot, W. G. Sawyer, S. B. Sinnott, S. S. Perry, *Phys. Rev. Lett.* **102**, 186102 (2009).
- J.-A. Ruan, B. Bhushan, *J. Appl. Phys.* **76**, 5022 (1994).
- S. Fujisawa, E. Kishi, Y. Sugawara, S. Morita, *Phys. Rev. B* **51**, 7849 (1995).
- K. Nakada, M. Fujita, G. Dresselhaus, M. S. Dresselhaus, *Phys. Rev. B* **54**, 17954 (1996).
- M. Y. Han, B. Ozyilmaz, Y. Zhang, P. Kim, *Phys. Rev. Lett.* **98**, 206805 (2007).
- M. Cieplak, E. D. Smith, M. O. Robbins, *Science* **265**, 1209 (1994).
- B. N. J. Persson, A. I. Volokitin, *J. Chem. Phys.* **103**, 8679 (1995).
- A. P. Merkle, L. D. Marks, *Tribol. Lett.* **26**, 73 (2007).
- K. R. Shull, *Mater. Sci. Eng. Rep.* **36**, 1 (2002).
- M. H. Müser, *Europhys. Lett.* **66**, 97 (2004).
- L. Prandtl, *Z. Angew. Math. Mech.* **8**, 85 (1928).
- We acknowledge support from the NSF under awards NSF/MRSEC (no. DMR-0520020) (R.W.C.), CMMI-0800154 (R.W.C.), CHE-0117752 (J.H.), and CMMI-0927891 (J.H.); the New York State Office of Science, Technology, and Academic Research (NYSTAR) (J.H.); the Defense Advanced Research Projects Agency (DARPA) Center on Nanoscale Science and Technology for Integrated Micro/Nano-Electromechanical Transducers (iMINT, grant HRO011-06-1-0048) (J.H.); Air Force Office of Scientific Research (AFOSR) (MURI FA955009-1-0705) (J.H.); and the Swiss NSF and its National Centers of Competence in Research (NCCR) MaNEP (H.B.). We thank Momentive Performance Materials, Advanced Diamond Technologies, and C. H. Lui for supplying h-BN powder, diamond-coated AFM probes, and graphene samples on mica, respectively. We acknowledge helpful discussions with J. Li, M. Müser, and L. Forró.

Supporting Online Material

www.sciencemag.org/cgi/content/full/328/5974/76/DC1
Materials and Methods
Figs. S1 to S8
References

3 November 2009; accepted 17 February 2010
10.1126/science.1184167

A Stratified Redox Model for the Ediacaran Ocean

Chao Li,^{1*} Gordon D. Love,¹ Timothy W. Lyons,¹ David A. Fike,² Alex L. Sessions,³ Xuelei Chu⁴

The Ediacaran Period (635 to 542 million years ago) was a time of fundamental environmental and evolutionary change, culminating in the first appearance of macroscopic animals. Here, we present a detailed spatial and temporal record of Ediacaran ocean chemistry for the Doushantuo Formation in the Nanhua Basin, South China. We find evidence for a metastable zone of euxinic (anoxic and sulfidic) waters impinging on the continental shelf and sandwiched within ferruginous [Fe(II)-enriched] deep waters. A stratified ocean with coeval oxic, sulfidic, and ferruginous zones, favored by overall low oceanic sulfate concentrations, was maintained dynamically throughout the Ediacaran Period. Our model reconciles seemingly conflicting geochemical redox conditions proposed previously for Ediacaran deep oceans and helps to explain the patchy temporal record of early metazoan fossils.

Numerous lines of geochemical and stable isotopic evidence have indicated that the Ediacaran (635 to 542 million years ago) ocean underwent a stepwise and protracted oxidation [e.g., (1–4)]. Some geochemical studies suggested that ocean basins were fully oxygenated by the late Ediacaran (1, 2, 4), yet others provided seemingly conflicting evidence for anoxic deep

waters (5, 6), with ferruginous conditions [Fe(II)-enriched] persisting into the Cambrian (5). Although a stratified ocean maintained through the Ediacaran Period (7) may help reconcile these seemingly conflicting views, the details remain unclear.

The Doushantuo Formation in the Nanhua Basin, South China, presents a unique opportunity to study Ediacaran ocean chemistry across spatial and temporal scales [e.g., (8)]. It is composed of a succession of both shallow- and deep-water siliciclastic, carbonate, and phosphatic sedimentary rocks deposited immediately after the last globally extensive Neoproterozoic glacial episode (9), widely known as the Marinoan glaciation. Zircon U-Pb ages indicate that the deposition of Doushantuo Formation lasted from ~635 to ~551 million years ago (10), spanning most of the Ediacaran Period.

To investigate the marine redox structure, we characterized the composition of sedimentary Fe mineral species and measured S isotope signatures for sulfides and sulfates (11) at four sections of Doushantuo Formation, which encompass the full range of sedimentary facies from continental shelf to slope to deep basin (fig. S1). We focused on quantifying the fractional abundance of Fe in several highly reactive mineral species (Fe_{HR}): pyrite (Fe_{Py}), Fe(III) oxides, magnetite, and carbonate minerals relative to total Fe (Fe_T) contents. High Fe_{HR}/Fe_T ratios indicate anoxic conditions (12). If anoxic, low associated Fe_{Py}/Fe_{HR} ratios indicate ferruginous bottom waters, whereas high Fe_{Py}/Fe_{HR} points to euxinic conditions, defined as having an anoxic and H₂S-containing water column (5, 12). In most modern and ancient sediments deposited beneath anoxic bottom waters, Fe_{HR}/Fe_T exceeds 0.38, but this threshold value can be reduced to 0.15 [±0.10 (SD)] for thermally altered ancient sedimentary rocks (13) such as Doushantuo Formation because of conversion of Fe_{HR} to nonreactive iron during burial. For a euxinic water column, Fe_{Py}/Fe_{HR} in the underlying sediments usually exceeds 0.8 (12). Previous Fe speciation data obtained from Paleoproterozoic and Mesoproterozoic sedimentary rocks (14, 15) revealed two distinct redox end members in marine basins characterized by either euxinic or ferruginous deep waters (fig. S2). In contrast, the iron speciation data from Doushantuo Formation are not confined to a single end member (Fig. 1A), suggesting nonuniform redox conditions for deep waters of Nanhua Basin.

The inner shelf Jiulongwan section records sedimentary deposition in the shallowest water

¹Department of Earth Sciences, University of California, Riverside, CA 92521, USA. ²Department of Earth and Planetary Sciences, Washington University, St. Louis, MO 63130, USA. ³Department of Geological and Planetary Sciences, California Institute of Technology, Pasadena, CA 91125, USA. ⁴State Key Laboratory of Lithospheric Evolution, Institute of Geology and Geophysics, Chinese Academy of Sciences, Beijing 100029, China.

*To whom correspondence should be addressed. E-mail: chaoli@ucr.edu